Electronic Supplementary Information for

Multiple crystal phases of intermetallic tungsten borides and phase-dependent electrocatalytic property for hydrogen evolution

Qiuju Li,‡ Lina Wang,‡ Xuan Ai, Hui Chen, Jiayun Zou, Guo-Dong Li* and Xiaoxin Zou*

State Key Laboratory of Inorganic Synthesis and Preparative Chemistry, College of Chemistry, Jilin University, Changchun 130012, P. R. China;

‡ Q. Li and L. Wang contributed equally to this work.

* E-mail: xxzou@jlu.edu.cn
lgd@jlu.edu.cn

1. Theoretical Section

1.1. Computation Details.

All the calculations were performed by using the Perdew-Burke-Ernzerhof (PBE)[1] exchange-correlation functional within the generalized gradient approximation (GGA) in the framework of *Vienna ab initio simulation package* (VASP)[2-3] based on the density functional theory (DFT). For all the structural relaxations and electronic structure calculations, the cutoff energy of plane-wave set[4] was 400 eV, while the convergence threshold was set as 0.02 eV/Å in force and 10^{-4} eV in energy. For the bulk calculations, the Brillouin zones were sampled by Monkhorst-Pack 7×7×7, 9×9×9, 4×4×5, 8×8×1, 9×9×3 and 7×7×5 k-point grid for Pt, W, W_2B, WB, WB_2 and WB_3, respectively. For the slab models, the appropriate Monkhorst-Pack *k*-point meshes 5×5×1 for Pt, W and WB_2, 4×4×1 for W_2B and WB, and 7×7×1 for WB_3 were employed. A 7×7×1 Monkhorst-Pack grid was used for the DOS calculations of slab models.[5] During the surface calculations, the symmetrization was switched off and the dipolar correction was included. The DFT-D2 method[6] was used to correct the *van der Waals* interaction. The crystal orbital Hamiltonian population (COHP) was obtained by LOBSTER code.[7-10]

We constructed the slab models by cleaving the bulk structure with metal-termination along the (001) direction for W_xB_y, the (110) direction for W and the (111) direction for Pt. The 1×1 supercells for W_2B and WB_3, 2×2 supercells for Pt, W, WB and WB_2 were employed, respectively. Among them, WB contains 8 metal atom layers and the other materials contain 4 metal atom layers. A vacuum layer of 15 Å between slabs was added to avoid inter-layer interactions, and the upper half of atom layers were relaxed while the remaining were kept frozen during the slab calculations.

1.2. Computations of Free-Energy for the Hydrogen Evolution Reaction.

The Gibbs free-energy (ΔG_{H^*}) of the hydrogen adsorption was calculated by the formula: $\Delta G_{H^*} = \Delta E_{H^*} + \Delta ZPE - T\Delta S$. ΔE_{H^*} is the adsorption energy, which is defined as $\Delta E_{H^*} = E(\text{surface} + \text{nH}) - E[\text{surface} + (\text{n-1})\text{H}] - 1/2\ E(H_2)$, where E(surface + nH), E[surface + (n-1)H] and $E(H_2)$ are the total energy of n, n-1 hydrogen atom adsorbed on the surface, and the energy of a gas phase H_2 molecule. ΔZPE and ΔS are the zero point energy and entropy change.[11] ΔZPE can be calculated by using the equation ΔZPE = ZPE (H*) – 1/2ZPE (H_2), and $T\Delta S$ can be obtained from the equation $T\Delta S \approx -1/2\ TS(H_2)$. It is worth mentioning that TS (H_2) is 0.41eV for H_2 at 298K and 1atm, the corresponding $T\Delta S \approx -0.205$ eV.

1.3. Computations of Density of States and *d*-Band Center.

The *d*-band center (ε_d) can be obtained by the formula:

$$\varepsilon_d = \frac{\int_{-\infty}^{\infty} n_d(\varepsilon)\varepsilon d\varepsilon}{\int_{-\infty}^{\infty} n_d(\varepsilon) d\varepsilon} \quad (1)$$

The *d*-band width (W_d) can be obtained by the formula:

$$W_d = \sqrt{\frac{\int_{-\infty}^{\infty} n_d(\varepsilon)(\varepsilon - \varepsilon_d)^2 d\varepsilon}{\int_{-\infty}^{\infty} n_d(\varepsilon) d\varepsilon}} \quad (2)$$

The upper band-edge energy (ε_d^W) was calculated by the following formula:

$$\varepsilon_d^W = \varepsilon_d + \frac{1}{2} W_d \quad (3)$$

where ε is the energy referring to E-Fermi and n_d (ε) is DOS projected onto *d*-states or different orbits of *d*-states.[12]

1.4. Computations of Formation Energy for Intermetallic Tungsten Borides.

The formation energies of intermetallic tungsten borides were calculated by the formula: ΔH_f = [$E_{total}(W_xB_y)$ - xE_{total}(W) - yE_{total}(B)]/(x+y), where $E_{total}(W_xB_y)$ is the total energy of one unit W_xB_y, E_{total}(W) and E_{total}(B) are the energies of pure metal W and α-B at the ground state, and x and y are the number of W and B atoms, respectively.

2. Experimental Section

2.1. Chemicals and Reagents.

Tungsten (VI) hexachloride (WCl_6, 99.9%) was purchased from Aladdin Chemistry Co., Ltd. Magnesium boride (MgB_2) was purchased from Alfa Aesar Chemicals Co., Ltd. Magnesium powder (Mg) was purchased from Shantou Xilong Chemical Factory. Isopropanol ($(CH_3)_2CHOH$) and Sulfuric acid (H_2SO_4) were purchased from Beijing Chemical Factory. Platinum on graphitized carbon (20 wt% Pt/C) and Nafion® perfluorinated resin solution were purchased from Sigma-Aldrich. Highly purified water (> 18 MΩ cm resistivity) was obtained from a PALL PURELAB Plus system.

2.2. Synthesis of Intermetallic Tungsten Borides.

All the chemicals were weighed under infrared light to avoid moisture influence. First, a certain amount of tungsten (VI) hexachloride (WCl_6), magnesium boride (MgB_2) and magnesium powder (Mg) were transferred into a quartz tube, which was then sealed in a vacuum atmosphere (1.0 Pa). The synthesis of WB_2 and WB_3 did not require the addition of Mg powder. Next, the sealed quartz tube was placed into a tube furnace and heated at a certain temperature. The heating rate and time are 2 °C min^{-1} and 5h, respectively. Please see the detailed synthetic parameters in Table S4. After cooling to room temperature, the product was ground into powder and dispersed in 0.5 M H_2SO_4 solution for 3 h to remove unreacted reactants (*i.e.*, Mg powder) and by-product (*i.e.*, $MgCl_2$). Finally, the resulting sample

was washed three times with distilled water and ethanol, respectively, and then oven-dried at 80 °C. WB_2 and WB were synthesized according to our previously reported methods.[13, 14]

2.3. Synthesis of W Nanoparticles.

0.5 mmol WCl_6 (198 mg) and 2 mmol Mg (46 mg) were put into a quartz tube, which was then sealed in a vacuum atmosphere (1.0 Pa). Then, the sealed quartz tube was placed into a tube furnace and heated at 600 °C for 4h, with a heating rate of 2 °C min^{-1}. After cooling to room temperature, the product was treated in the same method as the intermetallic tungsten borides.

2.4. Characterizations.

Powder X-ray diffraction (PXRD) of all samples were recorded on a Rigaku D/Max 2550 X-ray diffractometer with a scan speed of 7° min^{-1}, and the diffraction angle was from 10° to 80°. The transmission electron microscope (TEM) images were performed with a Philips-FEI Tecnai G2STwin microscope equipped with a field emission gun operating at 200 kV. The specific surface areas were obtained on a Micromeritics ASAP 2020 M system through the Brunauer-Emmett-Teller (BET) method. Xray photoelectron spectroscopy (XPS) was performed on an ESCALAB250 X-ray photoelectron spectrometer with a monochromatic X-ray source (Al Kα $h\upsilon$ = 1486.6 eV). Energy dispersive X-ray (EDX) analysis was obtained with an EDX system attached to JEOL JSM-7800F scanning electron microscope (SEM)

2.5. Electrochemical Measurements.

The electrochemical measurements were performed in a CH Instrument (Model 660E) with standard three-electrode system. The electrolyte was 0.5 M H_2SO_4 solution or 1 M KOH solution. Saturated calomel electrode (SCE) and Hg/HgO electrode were used as the reference electrodes in acidic and alkaline media, respectively. Carbon rod was used as the counter electrode. Glassy carbon electrode (GCE) loaded with catalyst was used as the working electrode. The working electrode was prepared by the fallowing steps: (1) 4 mg of catalyst was uniformly dispersed in 200 μL of isopropanol and 200 μL of conductive polymer binder (0.3% Nafion solution); (2) 2 μL of this solution was dropped onto a GCE with a diameter of 3 mm, and then dried in the air. The loading mass was 0.281 mg cm^{-2}; (3) 1 μL of 0.3% Nafion solution was dropped on top and dried.

During the measurements, N_2 was continuously passed into the electrochemical cell. Linear sweep voltammetry (LSV) measurements were performed with the scan rate of 1 mV/s and 85% *iR*-compensation. The 85% *iR*-compensations were obtained through positive feedback, according to the protocols reported recently by Jaramillo *et al.* [15, 16] Chronopotentiometric measurements were studied at a current density of 10 mA cm^{-2} without *iR*-compensation. The overpotentials required to reach 10 mA cm^{-2} current density at time t = 0 h and t = 2 h were obtained from chronopotentiometric curves. The catalytic activities of W nanoparticles and commercial 20 wt% Pt/C were tested under the same procedure.

The obtained potentials were converted to the potentials *vs* reversible hydrogen electrode (RHE) according to the formulas:

$$E_{vs.RHE} = E_{vs.SCE} + E^{o}_{SCE} + 0.059\,pH \qquad (4)$$

$$E_{vs.RHE} = E_{vs.Hg/HgO} + E^{o}_{Hg/HgO} + 0.059\,pH \quad (5)$$

where the E^{o}_{SCE} and $E^{o}_{Hg/HgO}$ were calibrated according to the method reported by Boettcher and co-workers.[17] The calibrated value were 0.261 V and 0.098V, respectively.

The geometric current density j_{geo} (mA cm^{-2}) was normalized by the geometric area of working electrode according to the formula:

$$j_{goe} = \frac{i \times 1000}{S} \quad (6)$$

where i (A) is the obtained current; S is the geometric area of working electrode (0.071 cm^2).

The specific activity j_{ECSA} (mA cm^{-2}) was normalized by the electrochemical active surface area (ECSA) according to the formula:

$$j_{ECSA} = \frac{i \times 1000}{ECSA} \quad (7)$$

where i (A) is the obtained current; ECSA is the corresponding electrochemical surface area of catalyst.

The ECSAs of catalysts were estimated from the values of their electrochemical doublelayer capacitance (C_{dl}), according to the method reported by Jaramillo and co-workers.[16] To obtain the C_{dl} of catalysts, cyclic voltammetry (CV) measurements were performed at non-faradaic potentials between –0.16 and –0.26 V *vs.* SCE with various scan rates (10, 20, 40, 60, 80, 100, 120 mV s^{-1}). By plotting the difference of anodic and cathodic currents ($i_{anodic} - i_{cathodic}$) at -0.21V *vs.* SCE against the scan rate, a linear trend was observed. C_{dl} is equal to half of the slope of the fitted line. The value of ECSA of catalyst on GCE was calculated according to the formula:

$$ECSA = \frac{C_{dl}}{C_s} \quad (8)$$

where C_s is the specific capacitance of the sample, and is estimated to be 0.035 mF cm^{-2} according to literature.[16]

The Faraday efficiency and electrochemical impedance spectroscopy (EIS) measurements were performed according to the procedures reported in our previous work.[18] In electrochemical impedance spectroscopy test, the initial potential at the working electrode was set as -0.2 V *vs.* RHE, and then a sinusoidal voltage with an amplitude of 5 mV and a scanning frequency of 10 kHz to 1 Hz were applied.

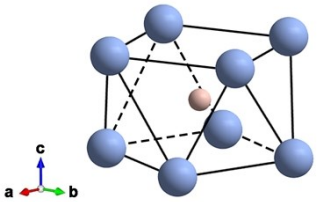

Fig. S1 Square antiprisms coordination of boron (pink ball) in W_2B.

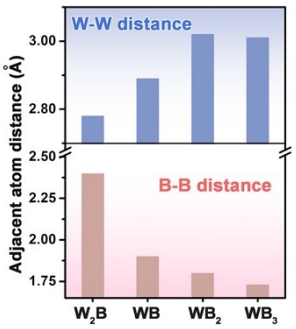

Fig. S2 The average distance of adjacent W-W and B-B atoms of four intermetallic tungsten borides.

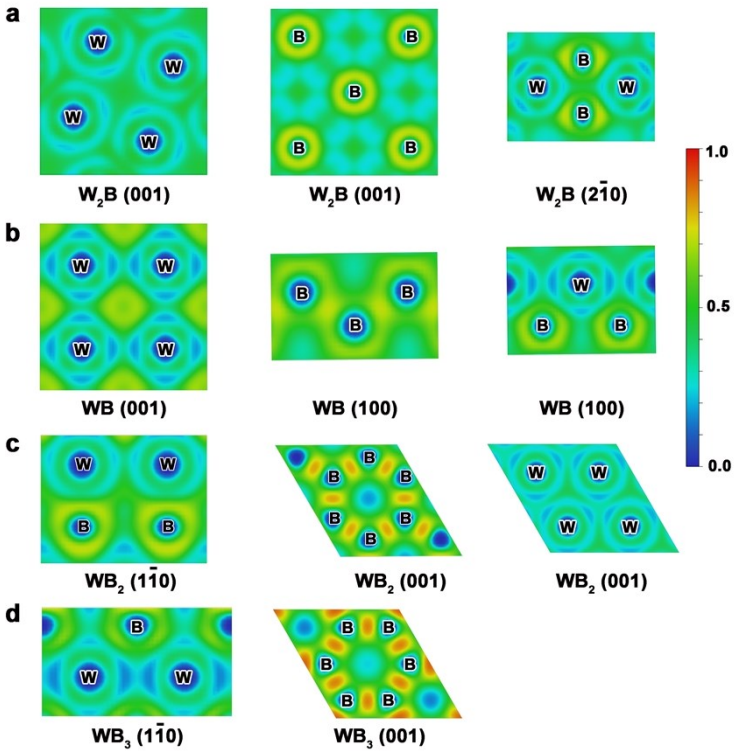

Fig. S3 ELF images of different planes for (a) W_2B, (b) WB, (c) WB_2 and (d) WB_3.

The electron location function (ELF) has been proven an effective tool to understand the nature of

the chemical bonding. By definition, the range of the ELF values is 0-1. The value close to 1 indicates the presence of covalent electrons or lone-pair electrons; the value of 0.5 represents a homogenous electron gas; the small value (near to 0) typically means the region between two electron shells.[19] In WB, WB_2 and WB_3, the ELF values are relatively large (0.8-0.9) between two adjacent B atoms, indicating the existence of strong B-B covalent bonds in them. The B-B distance is too long to form B-B bonds in W_2B. For W-W bonding, the correlative ELF values are in the range of 0.4-0.5, reflecting the electronic gas like those in metallic systems, indicating that W-W is metal bond in these tungsten borides. Finally, between adjacent W and B atoms, the electrons are gathered around the B atom, resulting in the formation of two electron shells. Therefore, the W-B bond is ionic.

Table S1 Bader charge transfer from W atom to adjacent B atoms in W_2B, WB, WB_2 and WB_3 (The positive and negative value indicate lose electron and get electron).

	W (*e*)	B (*e*)
W_2B	+0.47	–0.94
WB	+0.70	–0.70
WB_2	+1.00	–0.50
WB_3	+1.20	–0.40

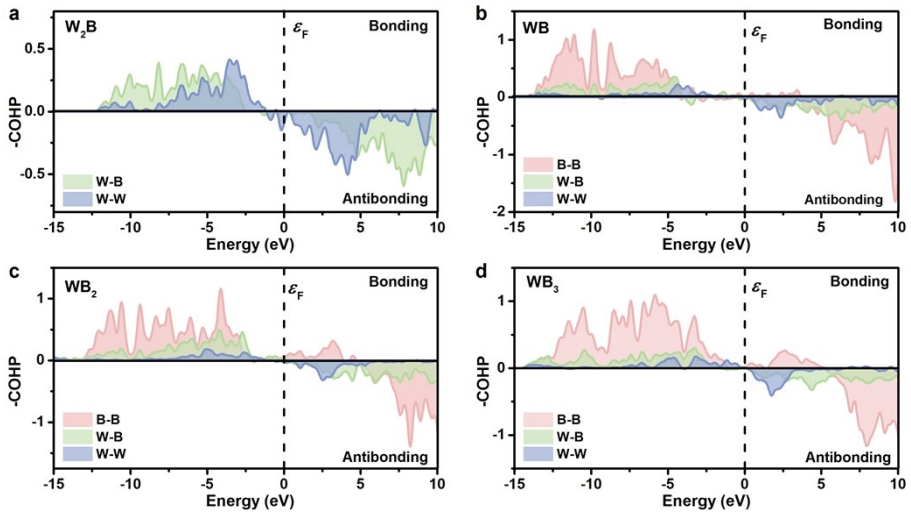

Fig. S4 COHP curves of (a) W_2B, (b) WB, (c) WB_2 and (d) WB_3.

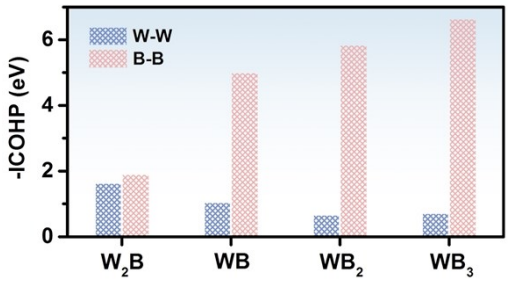

Fig. S5 The integrated COHP (-ICOHP) of W_2B, WB, WB_2 and WB_3 for different interactions.

Table S2 The integrated COHP (-ICOHP) of W_2B, WB, WB_2 and WB_3 for different interactions.

	B-B (eV)	W-W (eV)
W_2B	1.90	1.64
WB	5.00	1.06
WB_2	5.85	0.68
WB_3	6.65	0.73

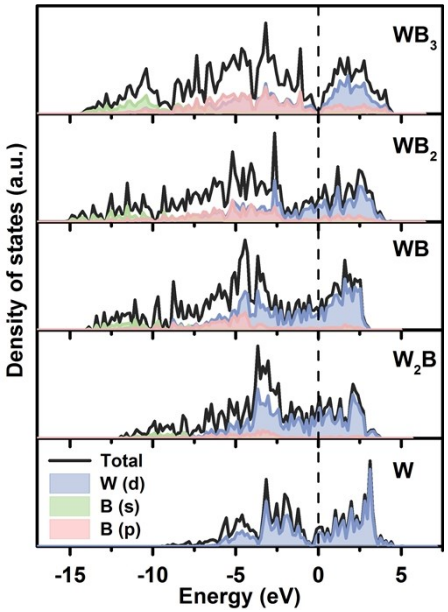

Fig. S6 Calculated DOS and pDOS of W, W_2B, WB, WB_2 and WB_3.

Table S3 The formation energies of four intermetallic tungsten borides.

	Formation Energy (eV/atom)
W_2B	-0.27
WB	-0.38
WB_2	-0.34
WB_3	-0.30

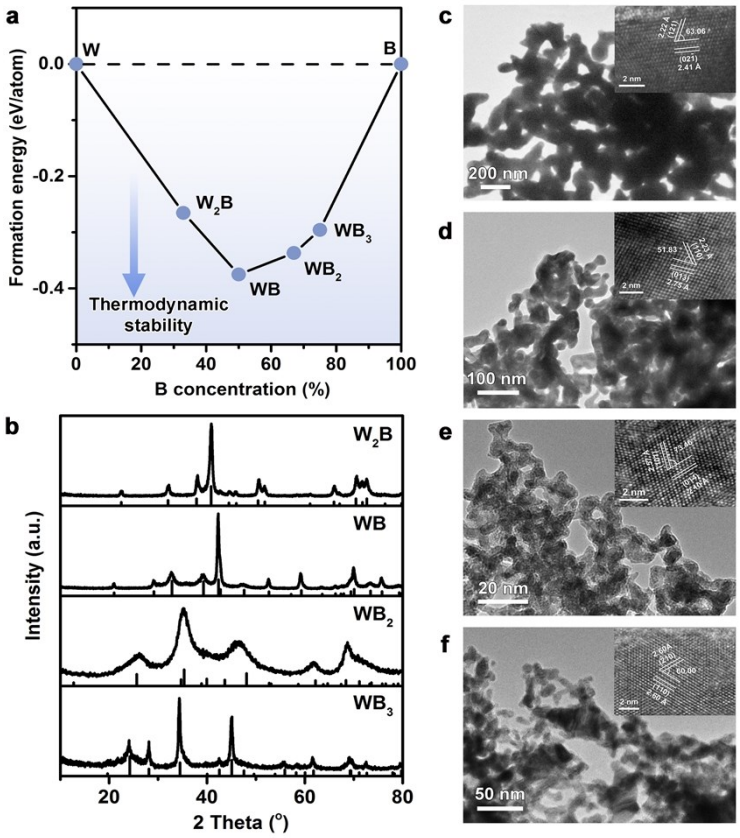

Fig. S7 (a) Convex hull diagram for the W-B system at 0 GPa. (b) The XRD patterns of intermetallic tungsten borides. For comparison, the standard XRD cards of W_2B, WB and WB_2 are included. The data for WB_3 peak positions derives from references.[20] TEM and high-resolution TEM images (insets) of (c) W_2B, (d) WB, (e) WB_2 and (f) WB_3.

Table S4. The experimental parameters for the synthesis of intermetallic tungsten borides.

Sample Name	WCl_6	MgB_2	Mg	Temperature and Time
W_2B	0.5 mmol	0.17 mmol	1.375 mmol	850 °C, 5h
WB	0.5 mmol	0.28 mmol	1.25 mmol	880 °C, 5h
WB_2	0.5 mmol	1.5 mmol	--	850 °C, 5h
WB_3	0.5 mmol	1.5 mmol	--	1150 °C, 5h

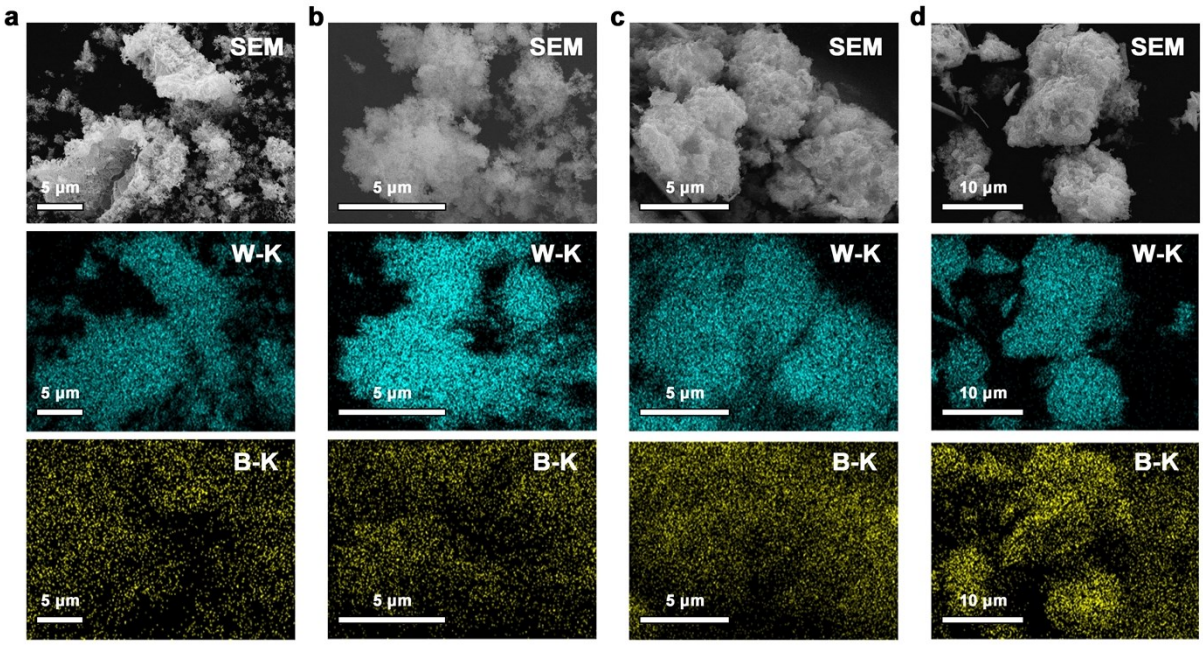

Fig. S8 The scanning electron microscopy-energy dispersive X-ray spectrometry (SEM-EDS) elemental mapping images of (a) W_2B, (b) WB, (c) WB_2 and (d) WB_3.

Table S5. The BET surface areas of the synthesized intermetallic tungsten borides.

	BET Surface Areas (m^2/g)
W_2B	5.5
WB	10.0
WB_2	18.6
WB_3	16.4

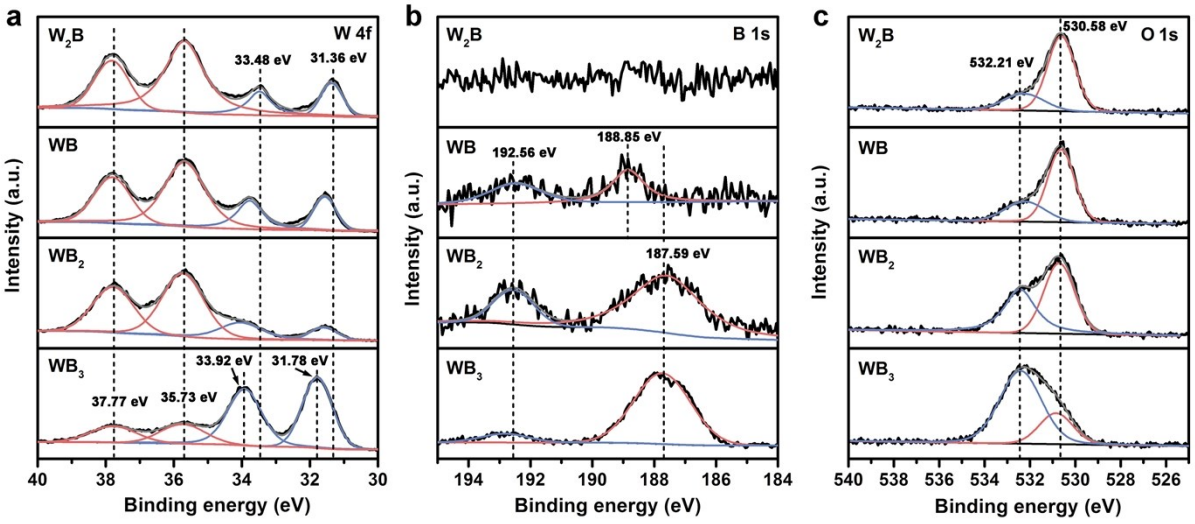

Fig. S9 (a) W 4f, (b) B 1s and (c) O 2p XPS spectra of four intermetallic tungsten borides.

The X-ray photoelectron spectroscopy (XPS) was performed to study the surface chemical states of W, B and O species for intermetallic tungsten borides. The W 4f spectra exhibit four peaks. The peaks at 35.73 eV and 37.77 eV are assigned to the W-O bonding, while the peaks at ~31.36 eV and ~33.48 eV are slightly shifted to the higher energy side compared with that of pure W (centered at 31 eV and 33.15 eV), which is related to W-B bonding.[21] Moreover, with the increase of boron content, the peaks related to W-B bonding upshift from 31.36 eV and 33.28 eV to 31.78 eV and 33.92 eV, respectively, indicating the enhancement of the W-B bonding. The B 1s peaks are located at 187.59 eV, 188.85 eV and 192.56 eV. The first two peaks are both assigned to boron, and the last peak is attributable to B-O bonding.[20] Note that due to the lowest boron content, the B 1s peaks in W_2B is not obvious. The O 1s spectra show two peaks at 530.58 eV and 532.21 eV, which come from O-W and O-B bonding, respectively.[22]

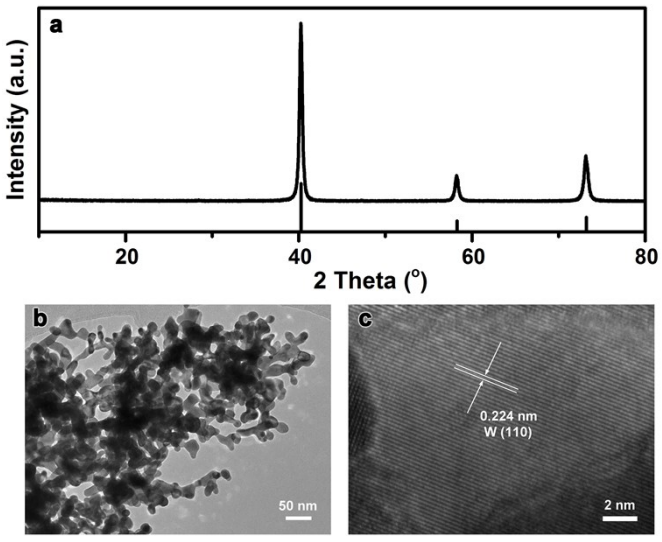

Fig. S10 (a) XRD pattern, (b) TEM image and (c) HRTEM image of W nanoparticles.

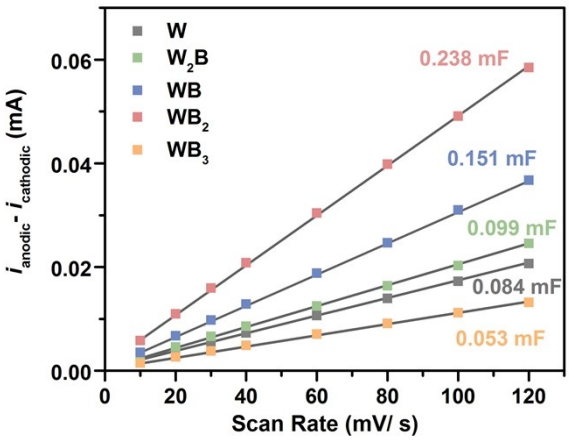

Fig. S11 The difference of current between the anodic and cathodic sweeps versus scan rate; half of the slope of the fitted line is equal to the electrochemical doublelayer capacitance (C_{dl}).

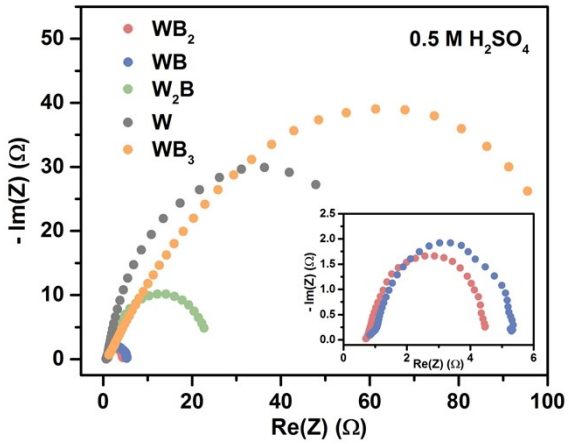

Fig. S12 Electrochemical impedance spectroscopy (EIS) Nyquist plots of intermetallic tungsten borides and W. The current densities are normalized with the geometric area of working electrode.

The electrochemical impedance spectroscopy is tested to determine the resistance and the interfacial electrode kinetics of materials. The result shows that all catalysts have similar R_s values, while R_{ct} values increase in the order of: WB_2 < WB < W_2B < W < WB_3. The smaller R_{ct} values, the faster electronic transport rates and more desirable catalytic kinetics.

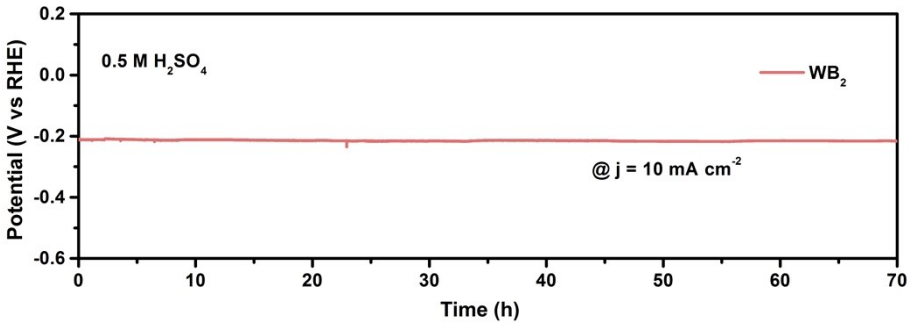

Fig. S13 Chronopotentiometric curves (without *iR*-compensation) of WB_2 at 10 mA cm_{goe}^{-2} in 0.5 M H_2SO_4 solution.

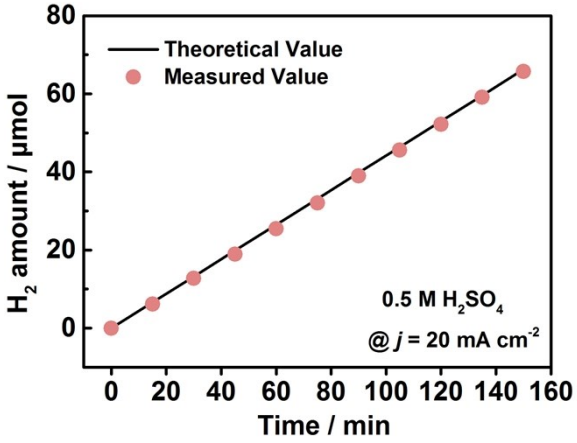

Fig. S14 Faraday efficiency of hydrogen production over WB_2 at a current density of 20 mA cm^{-2} in 0.5 M H_2SO_4 solution.

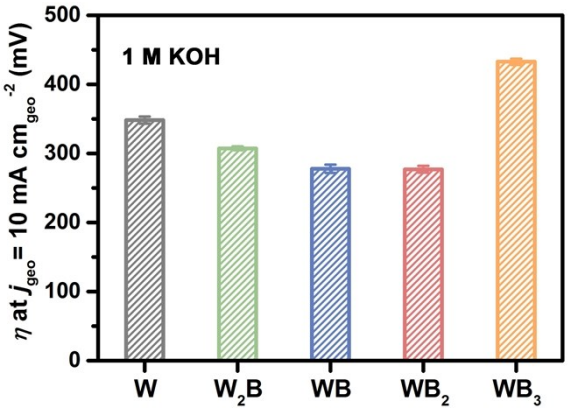

Fig. S15 Comparison of overpotentials at 10 mA cm_{geo}^{-2} (without *iR*-compensation) over intermetallic tungsten borides in 1 M KOH solution. Error bars indicate standard deviation from five measurements.

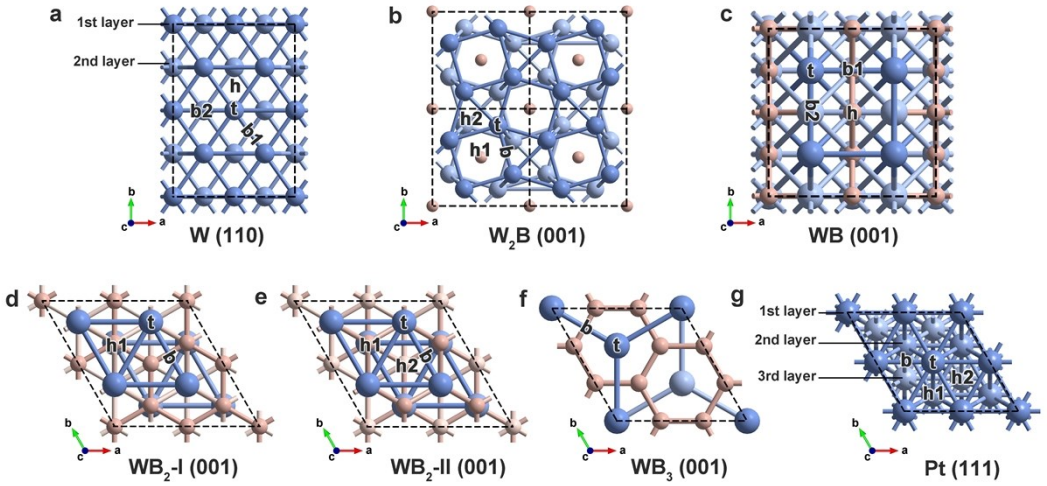

Fig. S16 The H*adsorption sites for (a) W (110), (b) W_2B (001), (c) WB (001), (d) WB_2-I, (e) WB_2-II, (f) WB_3 and (g) Pt (111) surfaces with metal-termination.

Table S6. The ΔE_{H^*} of WB_2-I, WB_2-II, WB_3, W_2B and Pt at different sites. The t, b and h denote the Top, Bridge and Hollow sites, respectively. The bolded values are ΔE_{H^*} in the most stable adsorption sites. WB_2-I and WB_2-II are W layers bond to graphene-like boron layers and puckered boron layers, respectively.

	t (eV)	b (eV)	h1 (eV)	h2 (eV)
WB_2-I	-0.65	-0.85	**-0.88**	--
WB_2-II	0.11	-0.98	-1.10	**-1.26**
WB_3	-0.87	**-1.38**	--	--
W_2B	Unstable	-0.90	-0.61	**-0.93**
Pt (111)	**-0.57**	-0.52	-0.49	-0.54

Table S7. The ΔE_{H^*} of WB and W at different sites. The t, b and h denote the Top, Bridge and Hollow sites, respectively. The bolded values are ΔE_{H^*} in the most stable adsorption sites.

	t (eV)	b1 (eV)	b2 (eV)	h (eV)
WB	-0.44	**-0.78**	-0.65	Unstable
W (110)	-0.20	-0.81	-0.66	**-0.86**

Table S8. The ΔG_{H^*} obtained at 100 % H* coverage on the most stable adsorption sites for different materials.

	ΔG_{H^*} (eV)
W_2B	-0.58
WB	-0.46
WB_2-I	-0.40
WB_2-II	-0.73
WB_3	-1.09
Pt (111)	-0.11
W (110)	-0.62

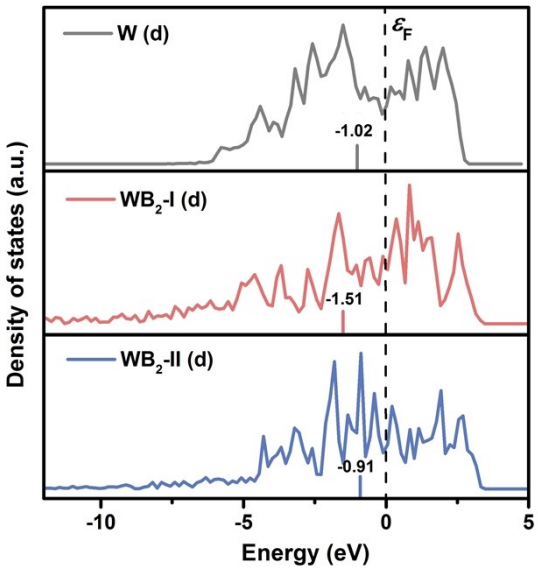

Fig. S17 The pDOS of d-states for the surface W atoms in the W, WB_2-I and WB_2-II slab models. The vertical line denotes the position of the Fermi energy, and colored bars indicate the *d*-band centers.

Table S9. The integrated COHP (-ICOHP) of W-B for the surface W atoms in the WB_2-I and WB_2-II slab models.

	-ICOHP (eV)	Coordination number	-ICOHP/unit cell (eV)
WB_2-I	2.05	6	12.30
WB_2-II	2.65	4	10.60

To reveal how the crystal phase affects the surface catalytic behaviors, we further tried to correlate the *d*-band center (ε_d) with the catalytic activity of intermetallic tungsten borides. However, there is no good consistency. This can be explained by the fact that the *d*-band center is a simple but not precise descriptor, and the *d*-band width (W_d) also affects the interaction energy. Thus, we used a slightly more advanced descriptor, $\varepsilon_d^W = \varepsilon_d + W_d/2$, the upper band-edge energy proposed by Nørskov at al.[12]

Table S10. The *d*-band center (ε_d), *d*-band width (W_d) and upper band-edge energy ($\varepsilon_d^W = \varepsilon_d + W_d/2$) for W_2B, WB, WB_2-I and WB_3 slab models.

	d-band center (eV)	*d*-band width (eV)	upper band-edge energy (eV)
W_2B	-1.27	2.92	0.19
WB	-1.75	3.28	-0.11
WB_2-I	-1.94	3.50	-0.19
WB_3	-1.28	3.62	0.53

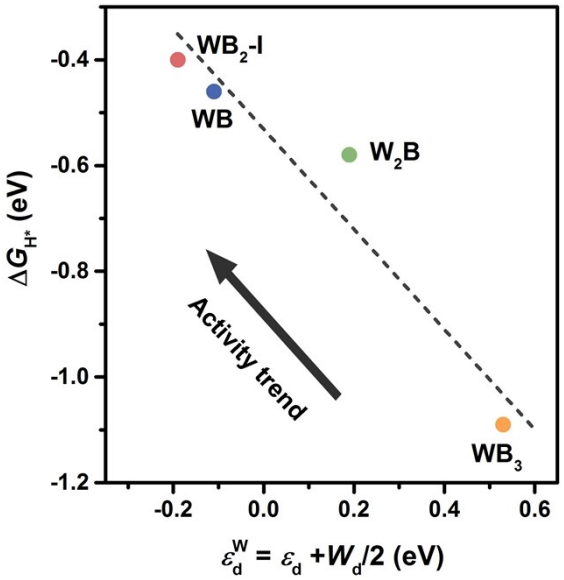

Fig. S18 Fitted linear relationship between ΔG_{H*} and upper band-edge energy of W_2B, WB, WB_2-I and WB_3.

Supplementary References

1. J. P. Perdew, K. Burke and M. Ernzerhof, *Phys. Rev. Lett.*, 1996, **77**, 3865.

2. G. Kresse and J. Furthmüller, *Comput. Mater. Sci.*, 1996, **6**, 15.

3. G. Kresse and J. Furthmüller, *Phys. Rev. B*, 1996, **54**, 11169.

4. P. E. Blöchl, *Phys. Rev. B*, 1994, **50**, 17953.

5. H. J. Monkhorst and J. D. Pack, *Phys. Rev. B*, 1976, **13**, 5188.

6. S. J. Grimme, *Comp. Chem.*, 2006, **27**, 1787.

7. R. Dronskowski and P. E. Blöchl, *J. Phys. Chem.*, 1993, **97**, 8617.

8. V. L. Deringer, A. L. Tchougreeff and R. Dronskowski, *J. Phys. Chem. A*, 2011, **115**, 5461.

9. S. Maintz, V. L. Deringer, A. L. Tchougreeff and R. Dronskowski, *J. Comput. Chem.*, 2013, **34**, 2557.

10. S. Maintz, V. L. Deringer, A. L. Tchougreeff and R. Dronskowski, *J. Comput. Chem.*, 2016, **37**, 1030.

11. J. K. Nørskov, T. Bligaard, A. Logadottir, J. R. Kitchin, J. Chen, S. Pandelov and U. Stimming, *J. Electrochem. Soc.*, 2005, **152**, 23.

12. A. Vojvodic, J. K. Nørskov, F. Abild-Pedersen, *Top. Catal.*, 2014, **57**, 25.

13. Q. Li, X. Zou, X. Ai, H. Chen, L. Sun and X. Zou, *Adv. Energy Mater.*, 2019, **9**, 1803369.

14. X. Ai, X. Zou, H. Chen, Y. Su, X. Feng, Q. Li, Y. Liu, Y. Zhang and X. Zou, *Angew. Chem., Int. Ed.,* 2020, **59**, 3961.

15. C. C. L. McCrory, S. Jung, J. C. Peters, T. F. Jaramillo, *J. Am. Chem. Soc.* 2013, **135**, 16977.

16. C. C. L. McCrory, S. Jung, I. M. Ferrer, S. M. Chatman, J. C. Peters and T. F. Jaramillo, *J. Am. Chem. Soc.,* 2015, **137**, 4347.

17. M. B. Stevens, L. J. Enman, A. S. Batchellor, M. R. Vise, A. E. Cosby, C. D. M. Trang and S. W. Boettcher, *Chem. Mater.,* 2017, **29**, 120.

18. Y. Liu, Q. Li, R. Si, G.-D. Li, W. Li, D.-P. Liu, D. Wang, L. Sun, Y. Zhang and X. Zou, *Adv. Mater.*, 2017, **29**, 1606200.

19. A. Savin, O. Jepsen, J. Flad, O. K. Andersen, H. Preuss and H. G. von Schnering, *Angew. Chem., Int. Ed.*, 1992, **31**, 187.

20. Q. Tao, D. Zheng, X. Zhao, Y. Chen, Q. Li, Q. Li, C. Wang, T. Cui, Y. Ma, X. Wang and P. Zhu, *Chem. Mater.*, 2014, **26**, 5297.

21. J. Chrzanowska-Giżyńska, P. Denis, S. Woźniacka and Ł. Kurpaska, *Ceram. Int.*, 2018, **44**, 19603.

22. Y. P. Xie, G. Liu, G. Q. Lu and H.-M. Cheng, *Nanoscale*, 2012, **4**, 1267.